Progress In Electromagnetics Research B, Vol. 69, 1–15, 2016

Modelling and Simulation of Conducted Emissions in the Powertrain of Electric Vehicles

Giordano Spadacini*, Flavia Grassi, and Sergio A. Pignari

Abstract—In the general framework of intelligent transportation, the increasing use of information-communication technology in full or hybrid electric vehicles requires careful assessment of electromagnetic compatibility, with specific reference to the conducted emissions (CE) generated by the inverter in a broad frequency range (10 kHz–100 MHz). To this aim, this work reports a modelling approach for the prediction of CE in electric powertrains, which is based on circuit representation of each single subsystem, that is, the battery, the inverter, the three-phase synchronous motor, and the power buses composed of shielded cables. The proposed models are able to represent both low-frequency functional aspects and high-frequency parasitic effects of paramount importance for CE analysis, and can be implemented into a Simulation-Programme-with-Integrated-Circuit-Emphasis (SPICE) solver. The proposed modelling approach is exploited to simulate virtual CE measurements according to international standard CISPR 25, and to investigate the impact of setup features, including grounding connections of shields, the propagation of CE in electrically long power buses, the operating point (power, torque, speed) of the motor-drive system.

1. INTRODUCTION

Nowadays, the automotive industry is facing a technological revolution driven by two major needs of the modern society. On the one hand, the pressure to lower carbon-dioxide emissions leads to the development of green vehicles, employing an electric powertrain as an alternative (hybrid vehicles) or substitute (full-electric vehicles) to the internal-combustion engine. On the other hand, the spread of revolutionary applications of information-communication technology (ICT) in all aspects of everyday life could not exclude transportation systems. Actually, modern cars involve increasing use of intelligent technologies made possible by digital electronic devices (e.g., processing units, sensors, etc.) installed aboard. Specifically, promising ICT applications are focused on optimal energy control, safety of road transport, connected vehicles, traffic decongestion, navigation services and info-mobility.

Unfortunately, the coexistence of signal interfaces and electric power systems in the relatively small volume of a car poses a significant technological challenge to designers committed to enforce and assess electromagnetic compatibility (EMC) [1]. Indeed, the electromagnetic environment in a hybrid/full electric vehicle is potentially hostile for the operation of susceptible electronic equipment, due to the presence of the inverter, that is the power-electronic circuit used to convert the direct current (dc) generated by the battery into the three-phase alternate current (ac) which feeds the motor, delivering powers of tens to hundreds of kilowatts. In order to explain the generation and propagation of electromagnetic noise inside the vehicle, Fig. 1 shows the general layout of an electric powertrain, where the electrochemical battery (in the rear compartment) is connected to the inverter (in the front compartment) through a long dc power bus running inside the vehicle chassis, having typical length of three to four meters. In turn, the inverter is connected to the nearby electric motor through a short (tens of centimetres) ac power bus.

Received 16 May 2016, Accepted 12 July 2016, Scheduled 19 July 2016
* Corresponding author: Giordano Spadacini (giordano.spadacini@polimi.it).
The authors are with the Dipartimento di Elettronica, Informazione e Bioingegneria, Politecnico di Milano, Milan, Italy.

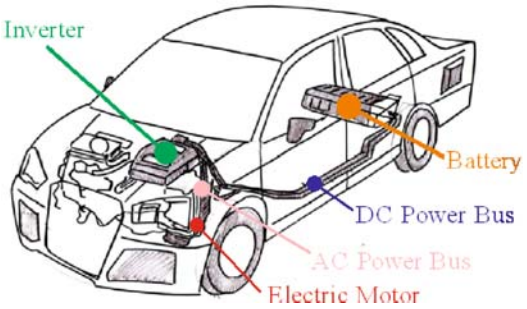

Figure 1. General layout of the electric-vehicle powertrain.

Automotive inverters involve Insulated-Gate Bipolar Transistors (IGBT) or other power-electronics devices operated at their maximum slew rate (typically, a switching frequency in the order of tens of kHz) so to reduce the current ripple in low-inductance compact motors and avoid acoustic noise due to vibrations in the audible frequency range. Such a fast switching of high dc currents (in the order of tens to hundreds Amps) implies the generation of noise currents, the so-called conducted emissions (CE), characterized by a rich spectral content in a broad frequency range extending from the fundamental switching frequency up to about 100 MHz. CE generated by the inverter propagate along the cables of the dc bus back to the battery. Although the dc power bus is composed of shielded cables to reduce interference effects, the conducted electromagnetic noise can efficiently couple onto susceptible circuits through crosstalk, or it can generate radiated electromagnetic fields in the resonating structure of the metallic chassis [2]. Finally, as a consequence of field-to-wire coupling, radiated disturbances may imply radiated-immunity problems to signal interconnects [2]. It is worth noting that also the ac power bus can conduct noise currents, however its reduced length and specific routing makes interference problems less important than those due to the dc power bus. As a partial list of susceptible electronic circuits whose operation may be impaired by the aforementioned electromagnetic disturbances one can cite (with increasing criticality): audio systems, car alarm and security, door switch modules, GPS navigation system, engine control units, antilock braking systems, air-bag control, collision-warning and avoidance controls.

The development of CE prediction models offers powerful analysis tools to EMC engineers for tailoring appropriate countermeasures in the early-design stage of the vehicle (e.g., implementation of filters, optimized layout of cables, etc.). In that respect, this work proposes a new circuit approach to the modelling of generation and propagation of CE in the dc power bus of electric vehicles.

One should firstly recognize that in the recent technical literature several works can be found devoted to circuit modelling of specific components of the electric-vehicle power system (e.g., battery, inverter, cables, motor). However, such models are targeted to heterogeneous objectives [3–8]. For instance, some models are devoted to functional, low-frequency aspects (e.g., control and operation of the motor) and are unable to account for high-frequency phenomena of interest for EMC [3]. Other models are specifically focused on the high-frequency behaviour, but they ignore functional aspects [4–7]. Moreover, some models are behavioural, black-box representations inferred from measurements [4, 5], while others are based on physical interpretation of the involved phenomena [6, 7].

To overcome these limitations, in this work selected models are suitably modified and integrated in order to harmonize different features and to ensure that the obtained model is representative both for functional aspects and for non-ideal parasitic effects typical of the high-frequency range. Specifically, circuit models for the battery, the inverter, and the permanent-magnet synchronous motor (PMSM) are derived, which can be easily implemented in a Simulation Programme-with-Integrated-Circuit-Emphasis (SPICE) software, which represents an industry standard for circuit simulation [8].

A similar approach was recently followed in [9], where a systematic analysis of CE in electric vehicles powertrain was successfully performed by integrating models of the inverter, the motor and the battery, to clearly put in evidence the interference-source mechanism. However, an important aspect was neglected in [9] and is here considered, namely, the impact of noise propagation along the dc power bus. Indeed, since the cable length results to be electrically long (i.e., comparable or

higher than the wavelength at the frequencies of interest), the propagation along the dc power bus considerably modifies the spectrum of CE [5]. In this regard, several literature works propose cable models based on lumped-equivalent multi-ports involving frequency-dependent impedances extracted from measurements [5, 10, 11]. Drawback of such a non-parametric approach stems from the fact that the obtained model is constrained to the specific cable geometry and arrangement (e.g., height of the cables above metallic ground, cable length, etc.) exploited for measurement, and cannot be generalized to different cable configurations. As shown in [12], a multiconductor-transmission-line (MTL) approach has to be used in order to properly account for propagation effects in electrically long cables. This distributed-parameter model were specifically developed in [13] for shielded cables used in automotive power buses. Though such a model is fully parametric, it cannot be represented by lumped-circuit elements in a SPICE solver. However, in this work it is shown that an optimized cascade of lumped-circuit cells can be derived from that model and integrated in SPICE, together with the aforementioned models of battery, inverter and PMSM. Such a cable model is here presented and experimentally validated.

The final result is a system-level circuit representation of the whole powertrain. Several SPICE time-domain simulations are performed to mimic the execution of CE measurements according to international standard CISPR 25 [14]. Effects of variations in the test setup are investigated, including lack of grounding of the cable shields, long-cable effects, and different operating points (power, torque, speed) of the motor.

2. CE TEST SETUP ACCORDING TO CISPR 25

In EMC testing, standardized test setups with controlled geometrical and electrical parameters are used to ensure repeatability of measurement results, and to establish reference test conditions allowing comparison of the performance of different systems. For measuring CE in electric-vehicle powertrains, standard CISPR 25 [14] foresees the test setup shown in Fig. 2. According to CISPR recommendations, all components of the power system shall be extracted from the vehicle and placed above a large metallic ground plane. Particularly, shielded cables shall be kept at a constant, controlled height h and distance d above ground, as shown in Fig. 3(a), where the cross section of the two shielded cables of the dc power bus is sketched. The metallic chassis of battery, inverter, motors, as well as the terminals of the cable shields, are connected to the ground plane (connections not detailed in Fig. 2).

A Line-Impedance Stabilisation Network (LISN), whose circuit model is shown in Fig. 3(b), as defined in CISPR 25, is connected at the interface between the battery and the dc power bus. The LISN standardizes the high-frequency impedance (10 kHz–100 MHz) seen by the dc power bus, so to make CE measurement independent from the specific battery or dc power source used in the test setup. In particular, at low, functional frequencies (dc) the inductors are short circuits and capacitors are open circuits, so that the battery is directly connected to the dc power bus (likewise in the absence of the LISN). Conversely, at the high frequencies of interest for CE, the impedances associated with the 5 µH inductors tend to become open circuits, whereas those of the 0.1 µF capacitors tend to become short circuits. As a result, the battery is decoupled from the power bus, and the equivalent impedance to ground (constant over frequency) coincides with the resistance of the 50 Ω resistors in Fig. 3(b). These resistors actually represent the ports of an instrument (a spectrum analyser, a receiver, or an oscilloscope), which enables the measurement of voltages V_1, V_2 [see Fig. 3(b)] defined as CE according to the CISPR 25 "voltage method" [14]. An alternative test procedure is the CISPR 25 "current-probe method," where the LISN is still present to stabilize the line impedance, but the spectrum analyser is connected to a current probe clamped on the dc power bus, allowing direct definition (and measurement) of CE in terms of noise currents flowing along the dc bus [14].

Circuit models for all components of the CISPR 25 test setup are presented in the following sections. Aim of the developed models is to properly represent both low frequency phenomena related to functional aspects and high-frequency phenomena related to the generation and propagation of CE.

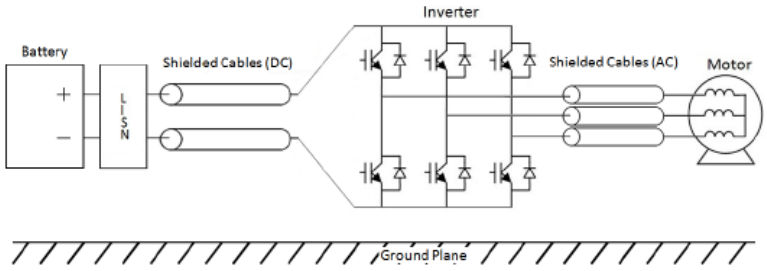

Figure 2. CISPR-25 CE test setup.

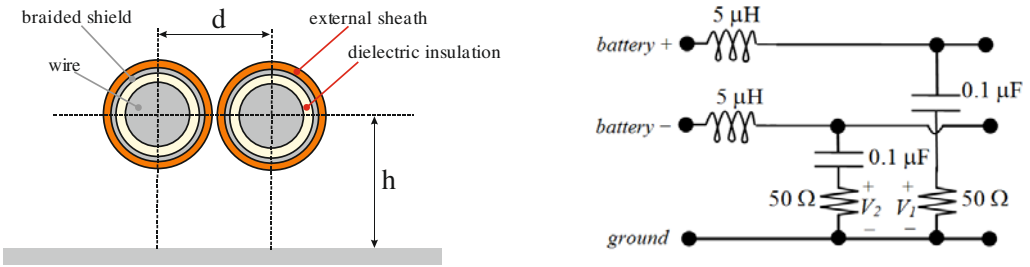

Figure 3. (a) Cross section of the dc power bus; (b) CISPR-25 LISN.

3. CIRCUIT MODELS OF FUNCTIONAL UNITS ACCOUNTING FOR HIGH-FREQUENCY EFFECTS

3.1. Circuit Model of the Inverter

The inverter model is shown in Fig. 4, where the external rectangle represents the metallic chassis. Two dc and three ac terminals are shown at the left and right side, respectively. Black elements in the circuit represent the basic functional components, that is: a) electronic valves (transistor T, diode D) arranged according to the so-called "three-leg" inverter structure [15], and b) the input capacitor C_{IM}. Other functional components (op-amp comparators, pulse generators, etc.) needed to synthesize and implement in SPICE the gate driving signals according to the Pulse-Width-Modulation (PWM) technique are not shown here, as they can be easily found in the technical literature [15].

These black components would not suffice to account for high-frequency phenomena of interest for CE prediction. As a matter of fact, in [4] it was shown that, in the frequency range 30 kHz–300 MHz, the inverter passive model is dominated by parasitic effects associated with the internal wiring structure, as well as with the involved power-electronics devices. In that work, an equivalent network was derived from scattering parameters measured in *ad hoc* test setups, whose dominant high-frequency parasitic components are here added to the inverter three-leg structure in Fig. 4 using the red color.

Inductor L_{IM} and resistor R_{IM} contribute to the non-ideal behaviour of the dc-bus capacitor, L_W are parasitic inductances of leg wires, C_H are parasitic capacitances connected between the inverter and its metallic housing.

Inductor L_{IGBT}, resistor R_{IGBT} and capacitor C_{IGBT} are parasitic components pertaining to the electronic valves and connected between the collector and the emitter. In this connection, it is worth noting that semiconductor manufacturers often make available SPICE sub-circuits models, which are very accurate in representing both the non-linear characteristics and parasitic effects of their power-electronics devices. In case these macro-models are available, they can be effectively used to substitute T, D, L_{IGBT}, R_{IGBT}, C_{IGBT} in Fig. 4.

Once specific values of these parameters are defined (strictly dependent on the inverter under analysis), the circuit in Fig. 4 is able to model both low-frequency operation and CE generation.

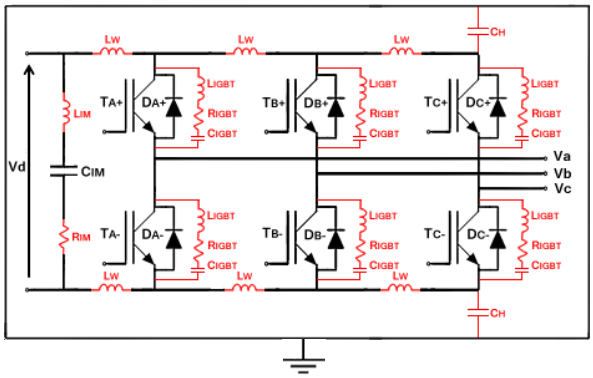

Figure 4. Circuit model of the inverter. The external black rectangle represents the metallic chassis, black circuit elements pertain to the functional low-frequency model, whereas red circuit elements describe high-frequency parasitic components.

3.2. Circuit Model of the PMSM

Harmonization of a low-frequency functional model with a high-frequency equivalent network is adopted also for PMSM modelling. The final result is shown in Fig. 5, where the external rectangle represents the metallic chassis (bonded to ground), black circuit elements pertain to the functional low-frequency model, whereas red circuit elements describe high-frequency parasitic components.

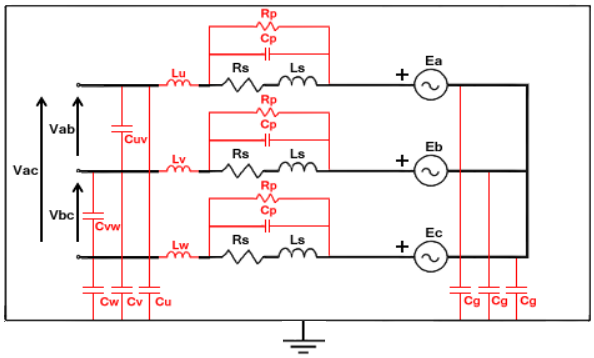

Figure 5. Circuit model of the PMSM. The external black rectangle represents the metallic chassis, black circuit elements pertain to the functional low-frequency model, whereas red circuit elements describe high-frequency parasitic components.

Concerning the functional part, one can recognize the classical topology of the steady-state model of three-phase synchronous electrical machines [3], involving the winding resistance R_S, the synchronous inductance L_S, and the back-electromotive force E. Specifically, while R_S, L_S are equal for all the three phases, back-electromotive forces E_a, E_b, E_c are equal in magnitude but shifted by a 120° angle. Suitably setting the amplitude and phase shift of E with respect to line voltages V_{ab}, V_{bc}, V_{ca} [3] allows enforcing a desired working point in the torque-speed characteristic of the motor.

Such a steady-state circuit cannot account for mechanical transients (e.g., starting from a stop, etc.) However, this limitation is in line whit CISPR-25 testing where only steady-state mechanical conditions are considered.

Concerning the non-ideal high-frequency behaviour of motors, a circuit model representative for relevant parasitic effects in the frequency range 100 kHz–500 MHz was firstly proposed in [6] with reference to an asynchronous configuration, and then refined and particularized in [7] for PMSMs used in electric-vehicle applications. The fundamental circuit components of such high-frequency model are drawn in red in Fig. 5. Inductances L_u, L_v, L_w and capacitances C_{uv}, C_{vw}, C_u, C_v, C_w are used to model parasitics of the motor plug, whereas R_p, C_p are associated with the non-ideal behaviour of the

stator coils at high-frequency. Finally, C_g is the parasitic capacitance between each coil and the motor housing.

3.3. Circuit Model of the Battery

The circuit model of the battery is shown in Fig. 6, where the external rectangle represents the metallic chassis (connected to ground), and V_{dc} represents the dc voltage source. Red circuit components (inductances L_s, L_c, capacitances C_c, C_{om}, C_g, and resistor R_{150}) are used to model the high-frequency behaviour of a Li-ion battery for automotive applications. This specific circuit topology has been inferred from [4], where measurements (in the frequency range 30 kHz–200 MHz) allowed synthesizing such a behavioural network, which provides the same frequency response of the battery at the external port. The fictitious inductor L_{ws} (suggested value 10 µH) is here added to decouple the dc source V_{dc} from the rest of the network at high frequencies (indeed, in the absence of this inductor, the ideal source would be a short circuit for high-frequency currents).

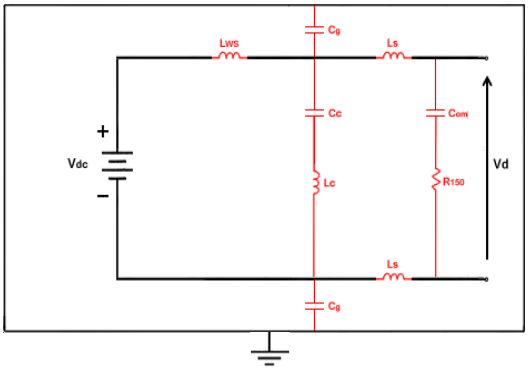

Figure 6. Circuit model of the battery. The external black rectangle represents the metallic chassis, black circuit elements pertain to the functional low-frequency model, whereas red circuit elements describe behavioral components modeling the high-frequency response.

4. CIRCUIT MODELS OF THE POWER BUS

Power buses composed of shielded cables play a significant role in the propagation of CE, since at the frequencies of interest they behave as MTLs, supporting different propagation modes with finite speeds. An MTL model is described here with reference to the dc power bus (model extension to the ac power bus is straightforward since it only requires to include an additional shielded cable).

4.1. MTL Model

The distributed-parameter circuit model of an infinitesimal line section (i.e., with length $\Delta x \to dx$) of dc power bus is shown in Fig. 7. In such a five-wire model, the first and third conductors represent the inner wires of coaxial cable No. 1 and No. 2, respectively, whereas the second and fourth conductors represent the shields. The lower conductor is the reference ground plane. Per unit length (p.u.l.) parameters are as follows: r_{W1}, r_{W2} denote the resistances of the inner wires; r_{S1}, r_{S2} the resistances of the two shields; L_{W1S1}, L_{W2S2} the mutual inductances between the shields and the inner wires; L_{W1}, L_{W2} the self-inductances of the inner wires; L_{S1}, L_{S2} the self-inductances of the shields; L_{WW}, L_{SS} the wire-to-wire and shield-to-shield mutual inductances, respectively; L_{S1W2} the mutual inductance between the inner conductor of the first cable and the shield of the second one (vice versa for L_{W1S2}); C_{W1S1}, C_{W2S2} are the mutual inductance between the shield and the inner wire; C_{S1}, C_{S2} the capacitances of each shield with respect to ground; finally, C_{S1S2} is the p.u.l. mutual capacitance between the shields. Due to the presence of the shields, some p.u.l. capacitances are null, that is: (a) the capacitances of the inner wires to ground; (b) the mutual capacitances between the inner wires; (c) the mutual capacitances

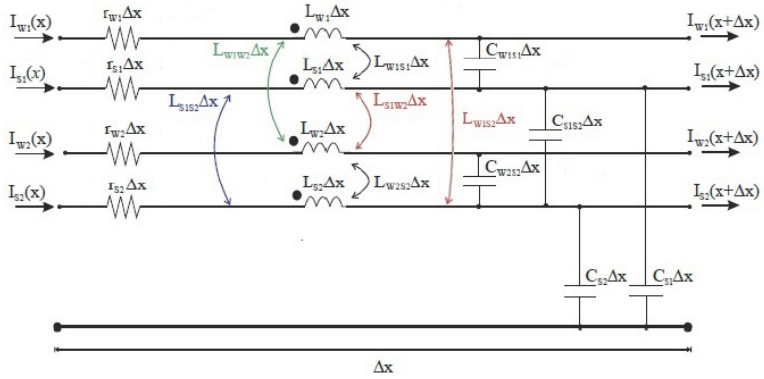

Figure 7. Circuit model of a section of length Δx of the dc power bus.

between the inner wire of a cable and the shield of the other cable. For the cross-section in Fig. 3(a), these parameters can be computed through electrostatic simulation and/or analytical expressions [13]. Note that, in general, p.u.l. resistances are frequency dependent due to skin effect [13].

Once the above p.u.l. parameters are known, the frequency-domain telegraphers' equations are written in compact matrix form as:

$$\begin{cases} \frac{d\mathbf{V}(x)}{dx} = -\mathbf{Z}\,\mathbf{I}(x) \\ \frac{d\mathbf{I}(x)}{dx} = -\mathbf{Y}\,\mathbf{V}(x) \end{cases} \tag{1}$$

where $\mathbf{V}$ and $\mathbf{I}$ are 4×1 column vectors of voltages and currents, respectively, at the generic position x along the MTL, and

$$\mathbf{Z} = diag\{r_W, r_S, r_W, r_S\} + j\omega \begin{bmatrix} L_{W1} & L_{WS1} & L_{WW} & L_{S2W1} \\ L_{WS1} & L_{S1} & L_{S1W2} & L_{SS} \\ L_{WW} & L_{S1W2} & L_{W2} & L_{WS2} \\ L_{S2W1} & L_{SS} & L_{WS2} & L_{S2} \end{bmatrix} \tag{2}$$

$$\mathbf{Y} = j\omega \begin{bmatrix} C_{WS} & -C_{WS} & 0 & 0 \\ -C_{WS} & C_{S1} + C_{WS} + C_{SS} & 0 & -C_{SS} \\ 0 & 0 & C_{WS} & -C_{WS} \\ 0 & -C_{SS} & -C_{WS} & C_{S2} + C_{WS} + C_{SS} \end{bmatrix}. \tag{3}$$

are the p.u.l. impedance and admittance matrices, respectively (j imaginary unit, ω angular frequency). Since solution of Eq. (1) is well known in the literature (for instance, see [16]), only specific steps of the solution process will be here recalled in order to evidence aspects of interest for the proposed work.

By deriving each member of the second MTL equations in Eq. (1), and by substitution of the first one, one yields the second-order differential equation [16]:

$$\frac{d^2\mathbf{I}(x)}{dx^2} = (\mathbf{YZ}) \cdot \mathbf{I}(x) \tag{4}$$

The matrix product $\mathbf{YZ}$ (full matrix) in Eq. (4) is then made diagonal by resorting to a similarity transformation matrix $\mathbf{T}$ so that

$$\mathbf{T^{-1}YZ\,T} = diag\{\gamma_1^2, \gamma_2^2, \gamma_3^2, \gamma_4^2\} \tag{5}$$

where γ_k^2, $k = 1, \ldots, 4$ represent the square of the propagation constants associated to the four modes propagating along the MTL. According to [2, 16], knowledge of the propagation constants γ_k and of the transformation matrix $\mathbf{T}$ (whose columns are the eigenvectors associated with the eigenvalues γ_k^2, $k = 1, \ldots, 4$) suffices to express the relationship between voltages and currents at the terminations of the cable of length $\mathscr{L}$ ($x = 0$ and $x = \mathscr{L}$) in the following form [16]:

$$\begin{bmatrix} \mathbf{V}(\mathscr{L}) \\ \mathbf{I}(\mathscr{L}) \end{bmatrix} = \begin{bmatrix} \mathbf{\Phi}_{11} & \mathbf{\Phi}_{12} \\ \mathbf{\Phi}_{21} & \mathbf{\Phi}_{22} \end{bmatrix} \cdot \begin{bmatrix} \mathbf{V}(0) \\ \mathbf{I}(0) \end{bmatrix} \tag{6}$$

where $\mathbf{\Phi}_{kh}$, $k, h = 1, 2$, are the so called "chain-parameter" sub-matrices of the MTL [16].

4.2. Lumped-circuit Approximation and Experimental Validation

Accuracy of the MTL model of the dc power bus was experimentally validated up to 100 MHz in [13]. However, the distributed-parameter model in Eq. (6) is not suitable for the aims of this work for a twofold reason. First, because it is a frequency-domain formulation, whereas circuit models for time-domain simulations are of interest in this work. Second, because sub-matrices $\mathbf{\Phi}_{kh}$ involve non-rational functions. Hence they cannot be modelled by lumped circuit elements in SPICE.

However, different approaches are possible for the implementation of MTL models in SPICE. A first method is the use of built-in approximate MTL models, possibly available in some commercial SPICE versions. A second method, available as long as losses are negligible (but it is not the case of this work) would be to resort to modal analysis and to the exact two-conductor transmission line models available in SPICE [2]. However, in order to account for losses, a third method is considered in this work, which is also not limited to specific SPICE versions and offers considerable advantages in terms of reduction of simulation time. The method is based on the approximation of the MTL by the cascade of several lumped-circuit cells exhibiting a Π-topology as shown in Fig. 8. In principle, for the definition of lumped frequency-dependent resistors (due to skin effect), one can resort to behavioral parts. However, since time-domain simulations will be of final interest here, we chose to neglect frequency dependence in order to avoid possible non-causality issues. Hence, we inputted constant resistances obtained as mean values in the frequency range of interest.

Evaluation of the optimal number of elemental Π cells requires a careful estimation on the basis of propagation properties of the MTL and the frequency band of interest. Indeed, an excessive number of cells would slow down the simulation time without increasing accuracy. Vice versa, an insufficient number of cells would lead to inaccurate results. As an example, let us consider the dc power-bus shown in Fig. 3(a), which is composed of two shielded copper cables (wire diameter 8 mm, insulation thickness 1 mm, shield thickness 0.5 mm, overall diameter 13.5 mm, relative permittivity of the insulation 2.35 and of the external sheath 7), running at height $h = 50$ mm and separated by a distance $d = 21$ mm. For this wiring, MTL analysis leads to the identification of four propagation modes with propagation constants $\gamma_k = \alpha_k + j\beta_k$ in Eq. (5), where the attenuation constants α_k are due to resistive losses, whereas phase constants β_k are related to the speeds of the four propagation modes as: $v_k = 2\pi f/\beta_k$ [16]. The maximum length (l_Π) of the elemental Π cells has therefore to be determined on the basis of the slowest velocity $v_{\min}$, so that at the maximum frequency ($f_{\max}$) the shortest wavelength $\lambda_{\min} = v_{\min}/f_{\max}$ results to be much larger than l_Π, that is: $l_\Pi \ll \lambda_{\min}$.

For the specific power cable here considered, and for $f_{\max} = 100$ MHz, the phase constants take the values: $\beta_1 = 3.3546\,\mathrm{s}^{-1}$, $\beta_2 = 3.3469\,\mathrm{s}^{-1}$, $\beta_3 = 2.1503\,\mathrm{s}^{-1}$, $\beta_4 = 2.1125\,\mathrm{s}^{-1}$. It turns out that the maximum phase constant is β_1, which corresponds to a slowest propagation speed $v_1 = 2\pi f/\beta_1 = 1.873 \cdot 10^8$ m/s. Therefore, the shortest wavelength takes the value $\lambda_{\min} = v_{\min}/f_{\max} = 1.873$ m. This example highlights that the dc power bus (whose typical length is about 3–4 m) is electrically long with respect to the minimum wavelength of interest involved in the propagation of CE, and stresses the importance of accurate cable modelling. A good rule of thumb for the discretization of an MTL suggests

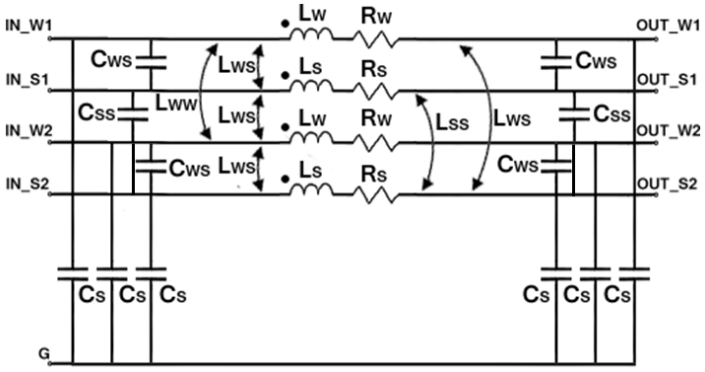

Figure 8. Elemental Π cell for the lumped-circuit approximation of the dc power bus.

the use of about 10 elemental lumped-circuit cells per wavelength [2, 16]. Therefore, the elemental Π cell in Fig. 8 will represent an MTL section of length $l_\Pi = \lambda_{\min}/10 = 18.7\,\text{cm}$ or less. Lumped inductances and resistances in Fig. 8 are obtained by multiplying the relevant p.u.l. parameters times l_Π. Conversely, since lumped capacitances are halved and splitted on both sides, their values are obtained by multiplying the relevant p.u.l. parameters times $l_\Pi/2$.

For the experimental validation of the proposed model, a power bus with length 2 m was considered and characterized at output ports by scattering-parameter measurements. A principle drawing and a picture of the test setup are shown in Fig. 9(a) and Fig. 9(b), respectively. Printed-circuit boards with SMA receptacles on both sides were designed to interface each coaxial cable with two separate ports (one for the inner wire W, and the other for the shield S) to be connected to the input ports of a Network Analyzer Agilent ENA E5071C. Measurements were carried out from 100 kHz up to 100 MHz. Selected scattering parameters measured (solid curves) and predicted (dashed curves) are shown in Fig. 9(c). For prediction, the SPICE model is modelled by the cascade connection of 12 lumped-Π elemental cells shown in Fig. 8 and referred to a length $2/12 = 16.7\,\text{cm} < 18.7\,\text{cm}$. The remarkable agreement between measurement and prediction proves model accuracy in the frequency range of interest.

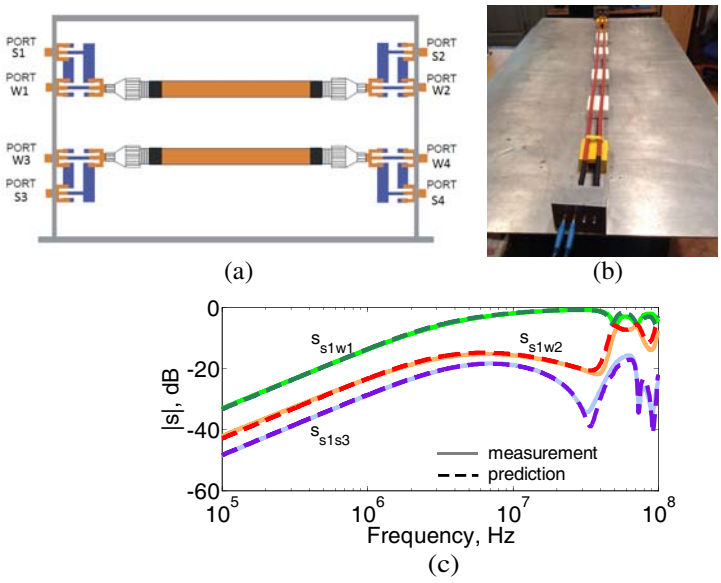

Figure 9. (a) Principle drawing and (b) picture of the experimental test setup for the characterization of power-bus scattering parameters. (c) Comparison of selected measurements versus predictions.

5. CIRCUIT MODEL OF THE WHOLE POWERTRAIN

5.1. Powertrain under Analysis

To exemplify the proposed modelling approach, a specific powertrain is considered in the remainder of this work. Data of functional units were inferred from the cited technical literature and are summarized in the following. The Li-ion electrochemical battery [5] generates a dc voltage $V_{dc} = 400\,\text{V}$, while behavioral high-frequency components are $L_s = 370\,\text{nH}$, $L_c = 320\,\text{nH}$, $C_c = 6.7\,\mu\text{F}$, $C_{om} = 330\,\text{pF}$, $C_g = 5.8\,\text{nF}$, $R_{150} = 150\,\Omega$ (see Fig. 6).

The inverter is composed of six IGBT valves IXIS 650V XPT (data sheet and SPICE model available in [17]), and an input capacitor $C_{IM} = 330\,\mu\text{F}$. Parasitic parameters are $L_{IM} = 8\,\text{nH}$, $R_{IM} = 1\,\text{m}\Omega$, $L_W = 50\,\text{nH}$, $C_H = 0.75\,\text{nF}$ (see Fig. 4) [4]. The inverted is driven by a PWM controller with switching frequency 34 kHz.

The three-phase PMSM has the following data referred to the nominal torque-speed working point: rated power 50 kW, line current 147 A (rms value), phase voltage 122 V (rms value), speed 3500 rpm,

frequency 117 Hz, power factor $\cos\phi = 0.95$. Values of functional parameters in the equivalent circuit of Fig. 5 are $R_S = 21\,\Omega$, $L_s = 0.4\,\text{mH}$, $E = 114\,\text{V}$ (rms value at the nominal torque-speed working point). Parasitic parameters are $L_u = L_v = L_w = 165\,\text{nH}$, $C_{uv} = C_{vw} = 4\,\text{nF}$, $C_u = C_v = C_w = 2.46\,\text{nF}$, $R_p = 457.5\,\Omega$, $C_p = 0.98\,\text{nF}$, $C_g = 0.62\,\text{nF}$ [7].

The dc power bus is composed of the two shielded cables previously described in Section 4.2, and leading to the following p.u.l. parameters (see Fig. 7): $r_{W1} = r_{W2} = 0.32\,\text{m}\Omega/\text{m}$, $r_{S1} = r_{S2} = 0.96\,\text{m}\Omega/\text{m}$, $L_{W1} = L_{W2} = 0.64\,\mu\text{H}/\text{m}$, $L_{S1} = L_{S2} = L_{W1S1} = L_{W2S2} = 0.58\,\mu\text{H}/\text{m}$, $L_{W1W2} = L_{S1S2} = L_{S1W2} = L_{W1S2} = 0.296\,\mu\text{H}/\text{m}$, $C_{W1S1} = C_{W2S2} = 464.6\,\text{pF}/\text{m}$, $C_{S1} = C_{S2} = 13\,\text{pF}/\text{m}$, $C_{S1S2} = 14.8\,\text{pF}/\text{m}$. The dc power bus has length 3.7 m and is modelled by the cascade connection of 20 lumped Π elemental cells as shown in Fig. 8.

The ac power bus is composed of three shielded cables with similar geometrical and electrical characteristics, and length 50 cm. Its MTL model is therefore obtained by including a third shielded cable that is two additional wires in the elemental Π-cell in Fig. 8, and is then implemented in SPICE by the cascade of three elemental cells.

5.2. SPICE Model

The proposed circuit models have been implemented in a commercial SPICE circuit solver [18]. Fig. 10 shows the resulting SPICE schematic obtained by connecting functional sub-circuits representing the battery, Fig. 6, LISN, Fig. 3(b), inverter, Fig. 4, motor, Fig. 5, and cascaded lumped-circuit cells pertaining to the power buses, Fig. 8.

Circuit simulations are performed in the time domain, from 0 ms to 120 ms, with variable time step automatically set by the SPICE algorithm to optimize convergence [18]. Voltages and current of interests are observed in a temporal window from 80 ms to 120 ms to ensure that a steady-state operating condition is reached (the smaller time constant of the dynamical system results about 20 ms and is due to the synchronous inductance of the motor). The obtained time-domain data are exported in an *ad hoc* post-processing software and transformed into frequency domain (via Fast Fourier Transform with Hanning window) so to obtain the spectrum of CE in the frequency range from 30 kHz up to 100 MHz. The computational time amounts to about 10 hours on a six-core CPU (Intel i7 3.33 GHz) equipped with 24-GB RAM. In this regard, the 10 elemental lumped-circuit cells per wavelength (here used to model power buses) represent a trade-off between accuracy and computational efficiency. Indeed, an increased number of cells per wavelength would lead to a higher order of the dynamic circuit, and the consequent increase of CPU time and memory allocation.

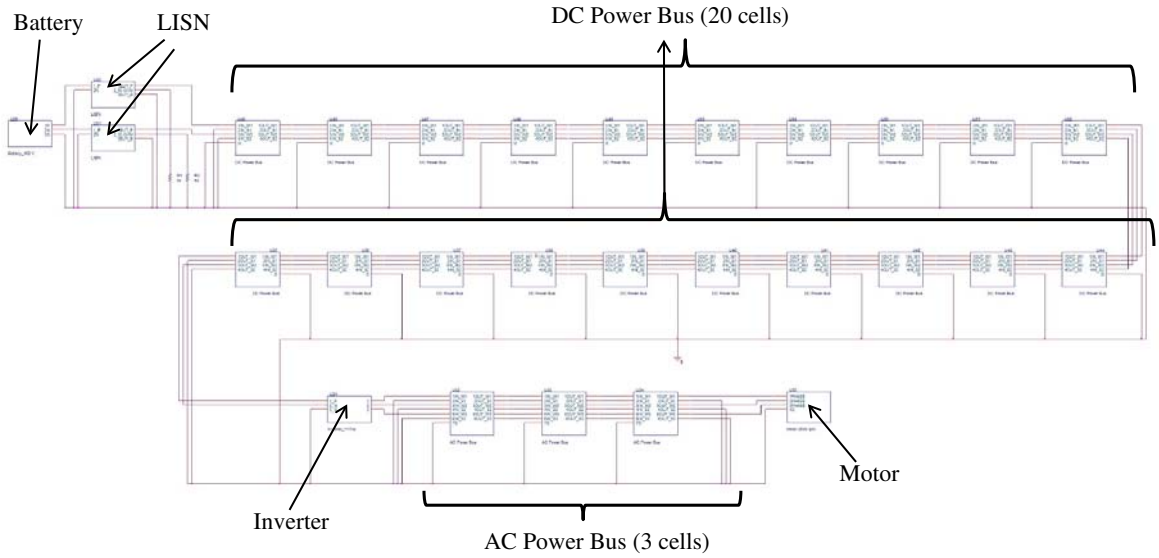

Figure 10. Implementation of the powertrain circuit model in SPICE.

6. SIMULATION RESULTS

In this section, several simulations are reported to demonstrate the effectiveness of the proposed modelling approach, and to investigate CE properties in different operating conditions.

6.1. Nominal Operating Point

In the first simulation, the PWM controller of the inverter [15], and the back-electromotive force of the motor [3], were properly set so to obtain the nominal frequency, nominal phase voltage and line current, corresponding to the nominal operating point, i.e., rated power 50 kW and torque 136.4 Nm at a speed of 3500 rpm (see detailed motor data in Section 5.1). The spectrum of CE evaluated by the CISPR voltage method is plotted in Fig. 11(a). Particularly, instead of directly plotting voltages V_1, V_2 evaluated at LISN terminals [see Fig. 3(b)], the modal voltages

$$V_{CM} = \frac{V_1 + V_2}{2}, \quad V_{DM} = \frac{V_1 - V_2}{2} \tag{7}$$

are considered. Decomposition of physical voltages V_1, V_2 into common-mode (CM) and differential-mode (DM) voltages in Eq. (7) is often used in EMC, since this fictitious set of voltages has the potential to put into evidence different propagation paths for CE noise, thus providing guidelines for filter design [2]. Specifically, DM noise circulates between the wires (plus and minus pin of the battery), whereas CM noise propagates in a closed loop formed by both wires and the metallic ground [2].

The spectrum of CE evaluated by the CISPR current-probe method is simulated in Fig. 11(b), that is, a current measured by a monitor probe clamped on the dc-power bus (sum of the four currents flowing in two inner wires and two shields). Particularly, the monitor probe is placed on the dc power-bus at two distances from the inverter: 1) 0 cm (i.e., at inverter connector) and 2) 75 cm.

The obtained CE spectra clearly show the presence of a first fundamental component at the inverter switching frequency (34 kHz), and all harmonic peaks (68 kHz, 102 kHz, 136 kHz, etc.) well above the noise floor up to 100 MHz. It is worth observing that CM voltage in Fig. 11(a) is greater than the DM voltage (meanly 20 dB), except for the first and second harmonic. This confirms that the generation of CM interference is the dominant phenomenon in inverter-fed motor-drive systems [4, 5, 8–13]. Moreover, Fig. 11(b) highlights the importance of probe positioning in the CISPR current-probe method [14], if very-high frequency components of CE are of interest (above 30 MHz). Indeed, one can observe a reduction (6–10 dB) of the current level if the probe is placed at 75 cm from the inverter. This difference is a natural consequence of propagation effects in the dc power bus acting as an electrically long MTL.

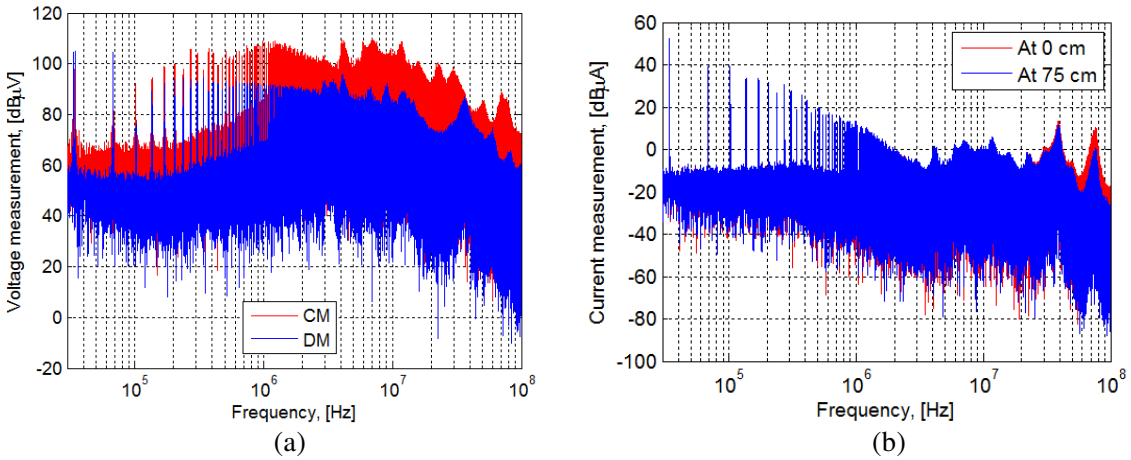

Figure 11. CE evaluated at the nominal operating condition of the powertrain: (a) CISPR voltage method with modal decomposition, (b) CISPR current-probe method at two different positions from the inverter.

6.2. Importance of Shield Grounding

In previous simulations, the test setup had both terminals of the two cable shields of the dc power bus grounded to the bottom metallic plane, as correctly required by the well-known EMC engineering practice [2]. It is here interesting to modify the proposed circuit model to show what happens if the shield of the dc power bus is not connected to ground (e.g., due to manufacture errors or the possible damage of grounding connectors). To this aim, the CISPR current-probe method is simulated (with the current probe at 0 cm from the inverter), and the obtained current spectrum (red spectrum) is compared in Fig. 12(a) versus the one previously obtained (blue spectrum) with the shields bonded to ground. The comparison reveals a dramatic increase in CE levels (more than 100 dB, that is, five orders of magnitude), thus further stressing the need for shield grounding.

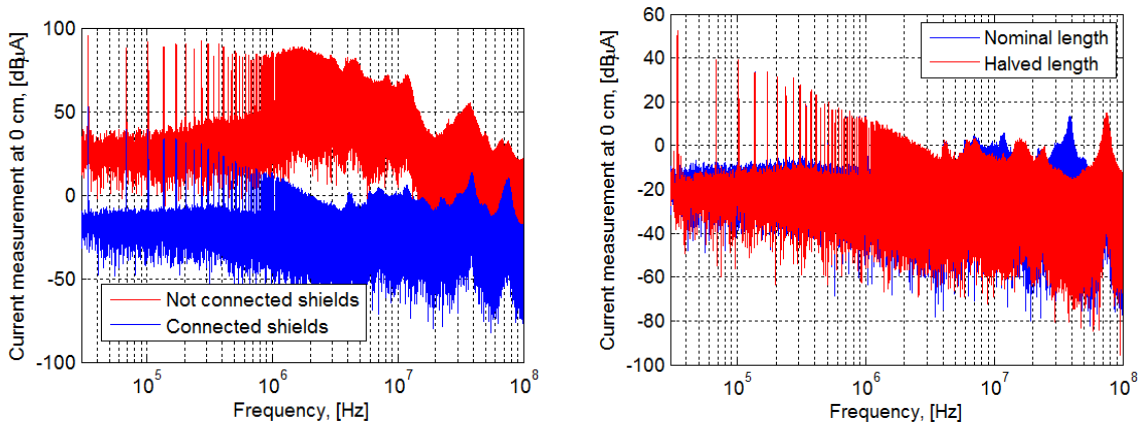

Figure 12. CE at the nominal operating condition of the powertrain (CISPR current-probe method): (a) Comparison of a test setup with proper grounding of cable shields, and a setup lacking ground connections; (b) Comparison of a test setup with nominal length of the dc power bus and a setup with halved length.

6.3. Impact of the Length of the dc Power Bus

The fundamental role of electrically long buses was mentioned in Section 4 to justify the development of a circuit model starting from a distributed-parameter representation. Actually, the impact of long-cable effects is fundamental in CE analysis of inverter-fed motor systems [5, 10–12], as well as other power-electronics devices such as dc/dc converters in space satellites [19, 20]. A quantitative estimation of the impact of the length of the dc power bus can be exemplified here by exploiting the proposed model.To this aim, the length of the dc power bus in Fig. 10 was halved (from 3.7 m to 1.85 m) by removing 10 lumped Π cells (out of a total number of 20). The CISPR current-probe method is simulated (current probe at 0 cm from the inverter), and the measured current is plotted in Fig. 12(b) where it is compared with the current obtained with nominal bus length (previously shown in Fig. 11). One can clearly observe that CE are not practically affected by the length of the power bus for frequencies less than 7 MHz. Conversely, above 7 MHz the test setup with halved length leads to a peak pattern shifted toward higher frequencies. In particular, the cluster of peaks around 38 MHz in the setup with nominal length is shifted around 76 MHz in the setup with halved length. Actually, these frequencies are resonances in the frequency response of the MTL [16], and have the detrimental effect of enhancing CE. This example confirms the fundamental role played by the power-bus impedance at high frequencies, as experimentally observed in [5].

6.4. Variation of the Operating Point

The CISPR 25 standard does not require specific operating points to be set in the torque-speed characteristics of the powertrain, and simply recommends careful documentation of testing conditions in the final test report. It is therefore interesting to investigate whether the power and speed of the motor have an actual impact on CE.

To this end, settings of the PWM controller of the inverter [15] and the back-electromotive force of the motor [3] were properly modified (with respect to Section 6.1) so to reproduce two different operating points according to the typical torque-speed characteristic used in the automotive industry [3]: a) reduced power 25 kW and rated torque 136.4 Nm at reduced speed of 1750 rpm; b) rated power 50 kW and reduced torque 101.8 Nm at increased speed 4690 rpm. Simulation results (CISPR voltage method, CM voltage component) are shown in Fig. 13(a) and Fig. 13(b), respectively, where they are compared with simulation results pertaining to the nominal operating point (previously shown in Fig. 11).

Red and blue curves plotted in Figs. 13(a)–(b) are mostly superimposed in the whole frequency range. By careful inspection, one can conclude that variations in the functional operating point of the powertrain (within limits of the typical torque-speed characteristic) have very limited effects on CE (variations of few dBs at specific frequencies). This finding supports the reasonability of the lack of requests in the current CISPR 25 standard, and assures repeatability of CE measurement even for different operating conditions of the powertrain.

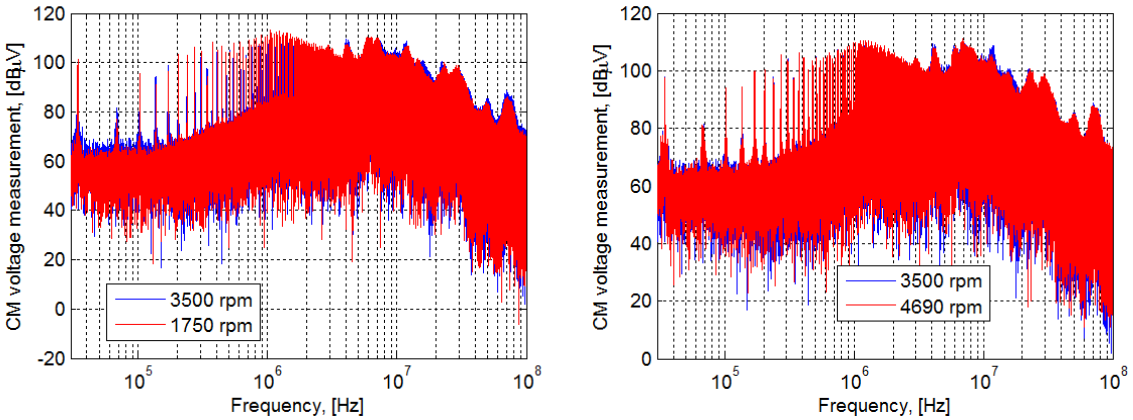

Figure 13. CE at the different operating conditions of the powertrain (CISPR voltage method, CM voltage): (a) reduced speed vs. nominal speed, (b) increased speed vs. nominal speed.

7. CONCLUSION

A circuit model for all subsystems (battery, inverter, motor) of an electric-vehicle powertrain was proposed, which is able to represent both the functional, low-frequency behaviour and high-frequency effects of interest for CE analysis. Additionally, a lumped-circuit approximation of power buses was derived from an accurate MTL representation. These models were integrated in a time-domain SPICE circuit solver, for the simulation of virtual CE measurements according to CISPR-25 voltage and current-probe methods.

Virtual CE measurements were used to investigate the impact of significant setup characteristics. Namely, the importance of using shielded cables with shield terminals properly connected to the metallic ground (i.e., to the car chassis in the on-board layout of Fig. 1) was confirmed. The shaping effect played by electrically-long dc power buses on the high-frequency portion of CE spectra was investigated. In particular, it was shown that MTL resonances (whose frequencies are strictly related to the line length) have the detrimental effect of increasing CE levels. Eventually, the negligible variation of CE with the powertrain operating point (power, torque, speed) was pointed out.

The proposed modelling approach represents a useful tool for the EMC-oriented design of electric-vehicle powertrains, as it allows easy identification of the main propagation paths of conducted disturbances. Different improvements and extensions are possible. As an example, the proposed SPICE representation of the power-bus could be easily integrated with circuit models of electromagnetic-interference filters (e.g., line-to-ground capacitors connected at the inverter dc input) for their effective design and system-level assessment [4]. Furthermore, by modifying the modulation technique exploited to control valve commutation (in this paper, a conventional PWM), it would be possible to evaluate its impact on EMC performance. Indeed, ongoing researches are currently aimed at the development of innovative modulation techniques able to reduce CE levels generated by inverter-fed power systems [21].

REFERENCES

1. Guo, Y. J., L. F. Wang, and C. L. Liao, "Modeling and analysis of conducted electromagnetic interference in electric vehicle power supply system," *Progress In Electromagnetic Research*, Vol. 139, 193–209, 2013.
2. Paul, C. R., *Introduction to Electromagnetic Compatibility*, Wiley & Sons, Inc., New York, 1992.
3. Staunton, R. H., S. C. Nelson, P. J. Otaduy, J. W. McKeever, J. M. Bailey, S. Das, and R. L. Smith, "PM motor parametric design analyses for a hybrid electric vehicle traction drive application," *Technical Report ORNL-TM-2004-217*, Oak Ridge National Laboratory, 2004.
4. Reuter, M., T. Friedl, S. Tenbohlen, and W. Kohler, "Emulation of conducted emissions of an automotive inverter for filter development in HV networks," *Proc. IEEE Int. Symp. on Electromagn. Compat.*, 236–241, Denver, CO, August 5–9, 2013.
5. Reuter, M., S. Tenbohlen, and W. Köhler, "The influence of network impedance on conducted disturbances within the high-voltage traction harness of electric vehicles," *IEEE Trans. Electromagn. Compat.*, Vol. 56, No. 1, 35–43, February 2014.
6. Boglietti, A. and E. Carpaneto, "Induction motor high frequency model," *Proc. IEEE Industry Applications Conference*, 1551–1558, 1999.
7. Pan, X., R. Ehrhard, and R. Vick, "An extended high frequency model of permanent magnet synchronous motors in hybrid vehicles," *Proc. EMC Europe 2011*, 690–694, York, UK, September 26–30, 2011.
8. Spadacini, G., F. Grassi, and S. A. Pignari, "SPICE simulation in time-domain of the CISPR 25 test setup for conducted emissions in electric vehicles," *Proc. APEMC 2015*, 569–572, Taipei, Taiwan, 2015.
9. Guo, Y. J., L. F. Wang, and C. Liao, "Systematic Analysis of conducted electromagnetic interferences for the electric drive system in electric vehicles," *Progress In Electromagnetic Research*, Vol. 134, 359–378, 2013.
10. Ran, L., S. Gokani, J. Clare, K. J. Bradley, and C. Christopoulos, "Conducted electromagnetic emissions in induction motor drive systems. Part I: Time domain analysis and identification of dominant modes," *IEEE Trans. Pow. Elect.*, Vol. 13, No. 4, 757–767, July 1998.
11. Revol, B., J. Roudet, J.-L. Schanen, and P. Loizelet, "EMI study of three-phase inverter-fed motor drives," *IEEE Trans. on Industry Applications*, Vol. 47, No. 1, 665–672, January/February 2011.
12. Ran, L., S. Gokani, J. Clare, K. J. Bradley, and C. Christopoulos, "Conducted electromagnetic emissions in induction motor drive systems. Part II: Frequency domain models," *IEEE Trans. Pow. Elect.*, Vol. 13, No. 4, 768–776, July 1998.
13. Beltramelli, A., F. Grassi, G. Spadacini, and S. A. Pignari, "Modeling conducted noise propagation along high-voltage DC power buses for electric vehicle applications," *Proc. ICCVE 2014, Int. Conf. on Connected Vehicles and Expo.*, 1–6, Vienna, Austria, November 3–7, 2014.
14. "Vehicles, boats, and internal combustion engines — Radio disturbance characteristics — Limits and methods of measurement for the protection of onboard receivers," *CISPR 25, IEC*, 2008.
15. Mohan, N., T. M. Undeland, and W. P. Robbins, *Power Electronics, Converters, Applications, and Design*, 2nd Edition, John Wiley & Sons, Inc., New York, 1995.

16. Paul, C. R., *Analysis of Multiconductor Transmission Lines*, John Wiley & Sons, Inc., New York, 1994.
17. IXYS Corporation, 650 V XPT Trench IGBTs GenX4, Model IXXN110N65C4H1 Data Sheet, 2013, PSPICE model available: http://www.ixys.com/TechnicalSupport/pspice.aspx.
18. Cadence Design Systems, Inc., Orcad Capture 16.6 User Guide, 2012.
19. Spadacini, G., F. Grassi, D. Bellan, S. A. Pignari, and F. Marliani, "Prediction of conducted emissions in satellite power buses," *International Journal of Aerospace Engineering*, 1–10, Article ID 601426, 2015.
20. Spadacini, G., D. Bellan, S. A. Pignari, R. Grossi, and F. Marliani, "Prediction of conducted emissions of DC/DC converters for space applications," *Proc. APEMC 2010*, 810–813, Beijing, China, April 12–16, 2010.
21. Liou, W.-R., H. M. Villaruza, M.-L. Yeh, and P. Roblin, "A digitally controlled low-EMI SPWM generation method for inverter applications," *IEEE Trans. Ind. Inf.*, Vol. 10, No. 1, 73–83, February 2014.